Science

RESEARCH ARTICLES

Cite as: D. H. Shugar *et al.*, *Science* 10.1126/science.aec3187 (2026).

A 481-meter-high landslide-tsunami in a cruise ship–frequented Alaska fjord

Dan H. Shugar[1]*, Katherine R. Barnhart[2], Mira Berdahl[3], Jacqueline Caplan-Auerbach[4], Göran Ekström[5], Aram Fathian[1], Marten Geertsema[6], Stephen P. Hicks[7], Bretwood Higman[8], Erin K. Jensen[2], Ezgi Karasözen[9], Patrick Lynett[10], John Lyons[11], Thomas Monahan[12], Gerard Roe[3], Kristian Svennevig[13], Liam Toney[2], Maximillian Van Wyk de Vries[14], Michael E. West[9]

[1]Water, Sediment, Hazards, and Earth-Surface Dynamics (waterSHED) Lab, Department of Earth, Energy, and Environment, University of Calgary, Calgary, AB, Canada. [2]US Geological Survey, Geologic Hazards Science Center, Golden, CO, USA. [3]Earth and Space Sciences Department, University of Washington, Seattle, WA, USA. [4]Geology Department, Western Washington University, Bellingham, WA, USA. [5]Lamont-Doherty Earth Observatory, Columbia University, Palisades, NY, USA. [6]Ministry of Forests, Prince George, BC, Canada. [7]Department of Earth Sciences, University College London, London, UK. [8]Ground Truth Alaska, Seldovia, AK, USA. [9]Alaska Earthquake Center, Geophysical Institute, University of Alaska Fairbanks, Fairbanks, AK, USA. [10]Department of Civil and Environmental Engineering, University of Southern California, Los Angeles, CA, USA. [11]US Geological Survey, Alaska Volcano Observatory, Anchorage, AK, USA. [12]Department of Engineering Science, University of Oxford, Oxford, UK. [13]GEUS, Geological Survey of Denmark and Greenland, Copenhagen, Denmark. [14]Complex and Multihazard Research Group (CoMHaz), Departments of Earth Sciences and Geography, University of Cambridge, Cambridge, UK.

***Corresponding author. Email: daniel.shugar@ucalgary.ca**

Early in the morning of 10 August 2025, a >64 × 10^6 m^3 landslide struck Tracy Arm fjord in Alaska. The landslide was preconditioned by glacial retreat caused by climate change. The resulting 481 m runup megatsunami followed an initial 100-m-high breaking wave traveling >70 m s^{-1}. The landslide was preceded by several days of microseismicity, which increased in rate and magnitude until ~1 hour before failure. The landslide produced globally observed long-period seismic waves equivalent in size to a M5.4 earthquake. A long-period (~66 s) global seismic signal, produced by a landslide-induced seiche trapped within the fjord, persisted for up to 36 hours, the second time a days-long seiche has been thus observed. With fjord regions increasingly visited by cruise ships, and climate change making similar events more likely, this unanticipated, near-miss event highlights the growing risk from landslides and tsunamis in coastal environments.

Landslide-generated tsunamis (hereafter referred to as landslide-tsunamis) can have substantially higher runups (the maximum height water reaches on a slope) than earthquake tsunamis, owing to larger, localized variations in water depth and direct water-column displacement by slope failure—most pronounced in confined water bodies like fjords. Since 1925, 27 landslide-tsunamis with runups ≥50 m have occurred (table S1), including most famously the 1958 Lituya Bay tsunami in southeast Alaska, which overtopped a ridge lying 530 m above sea level (asl) (*1*). That tsunami was generated by a ~30 × 10^6 m^3 landslide, itself triggered by a M7.8 earthquake (*2*). These cascading events unfold in minutes. Early detection of, and giving potential warning of, such rapidly cascading events is an ongoing scientific challenge.

Fjords with retreating tidewater glaciers are increasingly popular destinations for cruise ships and smaller vessels throughout the Arctic (*3*) and Subarctic, particularly in southeast Alaska. In the past few years, cruise ship passenger numbers in Alaska have increased from an annual average of ~1,000,000 in 2016 to ~1,600,000 in 2025 (*4*). Similarly, land-based recreation across the Arctic and Subarctic is increasing (*5*, *6*), resulting in greater exposure (and therefore risk) even in cases where the hazard is not increasing [e.g., (*7*)]. With enhanced retreat of glaciers (*8*, *9*) and permafrost degradation (*10*, *11*) due to climate change, however, the risk from large-scale landslide-tsunamis has increased substantially across the Arctic [e.g., (*12*)]. Landslide-tsunamis have already had serious consequences to Arctic communities, including loss of life and resettlement of entire communities (*10*, *13*, *14*), and are spurring risk reduction initiatives for communities and vessel operators in fjord environments (*15*).

Setting

Tracy Arm is a 50-km-long, ~1.3-km-wide, and up to 380-m-deep fjord, terminated by two tidewater glaciers: Sawyer Glacier and South Sawyer Glacier (Fig. 1), both fed by the Stikine Icefield (*16*). The steep-walled fjord is surrounded by peaks up to ~2000 m asl. The bedrock in Tracy Arm comprises the Coast plutonic complex (*17*), and the landslide site is mapped as migmatite consisting of schist, gneiss, and tonalite intruded by granodiorite (*18*). Permafrost is unlikely to be present (*19*, *20*). Tracy Arm was fully occupied by glacial ice at the Last Glacial Maximum, with a prominent moraine of unknown age formed at Holkham Bay, at the mouth of the fjord (*21*). High rates of thinning in recent decades have been documented for the Stikine Icefield and the adjacent Juneau Icefield (*8*, *22*, *23*), with considerable retreat on their outlet glaciers. Average thinning rates of about 1.0 m water

equivalent per year were reported in the vicinity of South Sawyer Glacier between 2000 and 2019, although thinning rates on lower South Sawyer Glacier itself are an order of magnitude higher (*24*). Snowline elevations were at about 1200 m asl in the early 1980s (*25*) and have risen by approximately 200 m since (*8*, *26*, *27*).

Juneau is the nearest sizeable community. During the summer months more than 20 boats per day visit the Tracy and Endicott arms. This includes up to six large cruise vessels per day, some of which carry as many as 6000 passengers and crew (*28*).

The landslide

Morphology, geometry, and volume

The landslide occurred at 5:26 AM local time (13:26 UTC) on 10 August 2025, in Tracy Arm at the terminus of South Sawyer Glacier (57.85°N, 133.07°W; Fig. 2). The headscarp was at ~1025 m asl (based on TopoBathyDEM; refer to materials and methods). Differencing of high-resolution pre- and post-event digital elevation models (DEMs) reveals a distinct wedge-shaped source, with a vertical thickness of up to 281 m and a slope-normal thickness of ~210 m (Fig. 2, C and D). The landslide source area is triangular in planform and can be reduced to three planes: a subvertical, ~82° striking, up to 180 m-high plane forming the headscarp, a 44°/159° (dip angle/dip direction) oriented eastern plane, and a 46°/214° oriented western plane. The landslide source thus had the geometry of a wedge with a maximum width of ~650 m near sea level. The subaerial portion of the total failed mass was at least 63.5 (+/−2.7) × 10^6 m^3, with a substantial volume of heavily disintegrated deposit material filling the northern side of the fjord in front of the glacier. As evidenced by ~150 m retreat of the coastline below the slope during the event, the basal rupture surface likely extended to an unknown depth below sea level. The ~64 × 10^6 m^3 is thus a minimum estimate of the total mobilized volume. Some primary landslide debris as well as dust was deposited on the terminus of the glacier (Fig. 2B and fig. S1). The apparent source-area structure and corresponding sense of movement classifies the initial landslide as a *rock wedge slide* (*29*). Initial landslide movement would have been translational and parallel to the intersection of the eastern and western planes (trend and plunge 182°/41°). Due to disintegration during transport, the landslide soon transitioned into a *rock avalanche* (*29*). Herein, we use the general term "landslide" to describe the failure (*30*).

Along both the west and east margins of the landslide, especially at elevations above 360 m and 435 m, respectively, the DEM-of-Difference exhibits net deposition (up to ~30 m thick, totalling about 0.6 × 10^6 m^3; table S2) (Fig. 2, C and D, blue arrows on right-most panels). These deposits appear to be outside of the main source area, indicating smaller landslides that might have occurred contemporaneously with, or slightly after, the main failure. Interpretation of seismic waveforms (fig. S1) and analysis of very-high-resolution satellite imagery (table S3) and oblique aerial photographs (*31*) indicate the debris west of a prominent ridge forming the western boundary of the main slide (fig. S2) failed ~6 min after the main landslide. As the main landslide moved downslope, it impacted the front of South Sawyer Glacier, covering ~0.4 km^2 of the remaining terminus of the glacier and resulting in the release of substantial quantities of ice into Tracy Arm, with some icebergs as large as ~0.1 km^2, as measured from Planet SuperDove imagery (table S3).

Pre-conditioning of the slope prior to the landslide

Although advance and retreat of tidewater-terminating glaciers can behave out of phase with land-terminating glaciers (*21*), most tidewater glaciers have retreated over the past two decades (*32*). South Sawyer Glacier has retreated throughout the 20th century, culminating in several episodes of rapid retreat separated by years to decades of stability. A nautical chart from 1898 (*33*) shows the north and south arms of the fjord nearly glacier-filled, and by the time aerial imagery was first collected in 1948 (table S3), South Sawyer Glacier had retreated about 3 km. By 1979 the glacier had retreated nearly another 3 km, where the face remained until 2004 when it retreated 1.7 km in a single year. The ice face remained largely stationary until 1.2 km of retreat occurred in 2016, where the ice face then remained until August of 2024. Minor retreat in the fall of 2024 was followed by re-advance, but in spring of 2025 retreat began again, ultimately exposing another 500 m of the north wall of the fjord. Only in July did retreat expose a portion of the base of the slope that would fail, and most of the pre-failure exposure occurred between 2 and 5 August. The landslide and tsunami, which impacted the glacier face, caused several hundred meters of additional glacier retreat.

Previous work estimated that the lower South Sawyer Glacier was thinning at a rate of about 4 m yr^{-1} (~0.65 km^3 yr^{-1}) between 1948 and 2000 (*34*), but substantially more since 2000. Melkonian *et al.* (*22*) report thinning rates of 17 to 19 m yr^{-1} in the frontal zone of South Sawyer Glacier between 2000 and 2013. At the site of the 2025 slope failure, the glacier thinned by approximately 100–130 m (equal to an average of 11–14 m yr^{-1}) between 2013 and 2022, according to ArcticDEM (*35*).

A relationship between fast glacier retreat and large landslide events has been observed elsewhere (*36*), such as for Grewingk Glacier lake in 1967 (*37*), Taan Fiord in 2015 (*38*), Elliot Creek in 2020 (*39*), Surprise Inlet in 2024 (*40*), and southern Greenland in the early Holocene (*41*). This trend suggests that glacial erosion had oversteepened the

subaerial slope since its last exposure, leaving it susceptible to glacial debuttressing as the South Sawyer Glacier retreated. However, due to an absence of proximal bathymetry data, we cannot be certain of either pre- or post-failure submarine slope geometries. The landslide occurred following several days of moderate rainfall (refer to supplementary text and fig. S3), but based on sparse station records (*42*, *43*), precipitation was not extreme leading up to the 10 August event.

The retreat and contraction of the region's glaciers is consistent with global patterns, which has been linked to increasing temperatures and consequent rising snowlines (*8*, *44*). We applied the attribution methodology of Berdahl *et al.* (*45*) to evaluate the cause of the warming (refer to materials and methods). From gridded observational datasets, there has been a 1.1 (+/− 0.14, 1σ) °C increase in summertime temperatures since the start of the industrial era (~1875), with much of that increase happening since the 1970s (fig. S4). This warming equates to an increase in the equilibrium line altitude of 169 (+/− 22, 1σ) m. By comparing the most recent (15 years) observed mean summertime temperatures with that of a large (~200-member) ensemble of naturally forced climate-model simulations (i.e., no anthropogenic forcing), we can estimate that the magnitude of the anthropogenic contribution to warming in this region is 1.1 +/− 0.3°C (1σ; fig. S4). Thus, the observed industrial-era warming appears entirely anthropogenic, in line with other global and regional assessments (*46*, *47*).

Precursory landslides

Retrospective analysis of optical and radar remote sensing shows no evidence of systematic pre-failure deformation on the primary slope that failed on 10 August 2025 (fig. S5). Very high-resolution (~0.5 m) imagery acquired on 22 June 2025 (i.e., 49 days before failure; refer to table S3) reveals no detectable tension cracks, scarps, or an incipient backscarp, implying that the slope failed with very little morphological warning. We did identify earlier, smaller slope failures: a ~25,000 m^2 translational failure occurred in the western sector in October 2017 and another in the eastern sector between 22–26 July 2025 with a runout of ~800 m (Fig. 2A). No seismic signals from these events were recorded on regional seismometers. Additional minor rockfalls are discernible in the latest available pre-slide Planet SuperDove image from 7 August 2025, which were not apparent on 6 August 2025 (Fig. 2A).

Precursory microseismicity

Retrospective analysis shows that regional seismometers (Fig. 1) recorded an increase in microseismicity at least 24 hours prior to the landslide at 13:26 UTC (05:26 local time) (Fig. 3A). The events became more frequent over time: on 9 August, they were recorded approximately every hour, but in the 6 hours prior to the slide event, they exhibited an exponential increase (Fig. 3A) with inter-event times between 30–60 s. The rate of these events decayed 1–2 hours before the landslide. However, seismic data indicate that at that moment the precursory events may have merged into continuous slip, with no discrete events but overall signal strength remaining well above background.

The onset of precursory seismicity associated with the Tracy Arm landslide is uncertain; the sparse seismic network in the area (Fig. 1) renders small events difficult to locate. We identified clusters of repeating earthquakes using waveform correlation and then stacked waveforms from events in each cluster to search for additional events with the same location and mechanism using template matching (Fig. 3). Fewer than 20 events were identified prior to 9 August, but some events were detected as early as 5 August. Similar precursory sequences — small, local, repeating earthquakes that increase in rate — have been detected prior to recurrent ice avalanches on Iliamna Volcano (*48*, *49*) and during landslides not involving ice (*50*, *51*). These precursory sequences likely represent stick-slip activity on small patches of the landslide failure plane, which can occur on ice and rock surfaces (*49*, *50*).

Seismic and infrasound signals from the main landslide failure

Forces associated with the main landslide generated seismic body- and surface-waves recorded at seismic stations around the world (Fig. 3B). An automatic global long-period surface-wave event detector (*52*) identified the landslide as a M5.4 seismic event, making it one of the largest-magnitude landslides globally in the last 30 years. More regionally, the Alaska Earthquake Center (AEC) runs a long-period, real-time landslide detection algorithm focused on Prince William Sound (*53*). Since 2023, this system has detected 35 landslides, but its search grid did not cover southeast Alaska. Following reports of a tsunami, the algorithm was applied to the region and obtained a preliminary location near South Sawyer Glacier (~7 km east of the subsequently confirmed source; Fig. 1), with a landslide volume estimate of 30–290 × 10^6 m^3 (fig. S6; refer to materials and methods). The landslide also produced infrasound waves clearly observed on five stations up to ~300 km away (fig. S7). We used an infrasound waveform back-projection method (*54*) to locate the landslide to within 10 km of the ultimately observed location (Fig. 1 and fig. S7; refer to materials and methods).

We used seismograms from regional and distant stations to determine the landslide-force history (LFH) and the corresponding trajectory of the landslide center of mass. Determination of the force history (fig. S8) was robust with respect to the selection of stations and seismograms included

in the inversion. The force history is relatively simple, with a total duration of approximately 2 min. The center-of-mass trajectory (fig. S9), obtained by integrating the force history twice, indicates an initial slide toward the south, later curving to the west. With an assumed center-of-mass displacement of 2000 m, the LFH results imply a mass of 370 million metric tons (approximately 142 × 10^6 m^3, assuming density of 2.6 g/cm^3), which is larger than that estimated from DEM differencing, likely due in part to the large volume of water mobilized by the landslide, or possibly to a component of submarine failure not captured in the DEM.

The tsunami

Eyewitness accounts

Several eyewitnesses in Tracy and Endicott arms observed the tsunami (refer to supplementary text). A group of kayakers camped on Harbor Island ~55 km from the landslide (Fig. 1) reported waking at 05:45 AKDT (13:45 UTC; 20 min post-landslide) to the sight of water flowing past their tent, carrying away one of their kayaks and much of their gear (*55*). Nearby, in No Name Bay ~50 km from the landslide, an observer on the motor vessel (M/V) Blackwood (Fig. 1) described a 6–8 foot (2–2.5 m) cresting wave coming along the beach from the direction of Tracy Arm, followed by a 3–4 foot (~1 m) wave (refer to supplementary text).

Observers aboard the small cruise boat M/V David B, anchored in Fords Terror, Endicott Arm ~85 km from the landslide (Fig. 1), described a surge of water pouring over a nearby sandbar, and witnessed the vessel rise ~3 m on the water despite a falling tide, still ongoing by ~06:15 AKDT (14:15 UTC; 50 min post-landslide). The crew reported continued surging at ~11:00 AKDT (19:00 UTC; ~5.5 hours post-landslide) when their skiff, anchored in shallow water near shore, was found to be on dry land only a few minutes later (refer to supplementary text).

At the time of the event, the cruise ship National Geographic Venture, carrying ~150 people, was anchored near the mouth of Tracy Arm (Fig. 1). At this location, the ship's captain described currents and white water near the edges of the fjord, but no obvious wave (refer to supplementary text). A significant amount of ice and debris was visible in the water, but their view of the fjord was hampered by dense fog.

Runup and geomorphic observations

As the tsunami propagated out of Tracy Arm, it stripped the fjord's walls of vegetation, leaving a trimline (Fig. 2, B, E, and F) similar to that left by the Taan Fiord tsunami in 2015 (*56*). In addition to the satellite imagery–identified trimline, we conducted a rapid-response field survey to measure runup/trimline elevations at accessible sites in mid-October 2025 (refer to materials and methods). The maximum tsunami runup, 481 m asl (+/− 7.6 m), observed from a helicopter-mounted altimeter, occurred on the south side of the fjord, ~3.3 km across from the landslide headscarp. This observation is consistent with a DEM-derived trimline elevation measurement of ~471 m above mean lower low water (MLLW) at about the same location. At the first major bend in the fjord, ~3 km west of South Sawyer Glacier terminus, the trimline reached 95–185 m elevation on the outer (southwest) fjord wall, and ~40–120 m elevation on the inner fjord wall. Like Cenotaph Island in Lituya Bay (*57*), a small patch of forest (ranging between 22 and 35 m above MLLW) on Sawyer Island, about 9 km from the landslide (Fig. 1), survived the tsunami (Fig. 2F). North of Sawyer Island, in the 0.3–0.5-km-wide northern branch of Tracy Arm, the tsunami removed vegetation to elevations exceeding 105 m locally and eroded the terminus of Sawyer Glacier. The most distal traces of tsunami runup and erosion are ~50–55 km from the landslide, in Holkham Bay (16 m elevation), a few km east of the kayaker camp, and at Williams Cove (35 m elevation from field survey; eyewitness video in auxiliary file S1 and fig. S10). The tsunami was recorded at two tide stations. A gage operated by JOA Surveys, with NOAA support (station ID 9452005, refer to Data, code, and materials availability), recorded the wave in Endicott Arm. A NOAA tide gage at Juneau, Alaska, ~130 km (tsunami travel distance) from the source area, was the most distal to record the tsunami and measured a peak amplitude of 0.4 m with the initial crest arriving 1 hour after the landslide and a dominant period of 20 min (1-min sampling interval).

Tsunami modeling

Integrating the calculated landslide volume, the seismic estimation of the landslide motion, and the satellite-derived runup heights, we developed a landslide-motion time history as a tsunami source. Using an ocean water simulator solving the nonlinear shallow water wave equations (*58*, *59*), the landslide mass was initialized on the slope, and the motion of the landslide was calibrated to reproduce the observed near-field runup within 3 km of the landslide (Fig. 4). The model also reproduces independent constraints, including trimline elevations throughout Tracy Arm (Fig. 4A), the approximate timing and elevations of the tsunami from eyewitness observations (Fig. 4B), the NOAA tide gage observation at Juneau (Fig. 4C), and the JOA tide gage in Endicott Arm (refer to location marker in Figs. 1 and 4B southeast of Fords Terror) showing a decaying seiche signal (Fig. 4D). As the model captures both near-field runup and far-field tide-gage observations, it provides a physically consistent bridge between extreme local effect and modest distal signals, which is used for post-event reconstruction and for evaluating what aspects of these signals could offer potential for warning and forecasts.

A tsunami-generation simulation (Movie 1) demonstrates that impulsive and efficient water-column displacement by the landslide would have produced a cross-channel-directed, intensely turbulent, white-water surge that dominated near-field maximum runup and flow speeds (approaching 70 m s^{-1}), consistent with the "Tsunami Opposite of the Slide" record in Fig. 4B and the near-source evolution in Movie 1 (refer to materials and methods for details on near-field crest heights, flow speeds, and timing). In addition to the cross-channel directed wave that generated the event-maximum runup, modeling indicates that the landslide sent a large tsunami to the northwest, traveling out through the fjord; this was the wave that caused the maximum runup throughout the rest of Tracy Arm (Fig. 4, A and B). Within minutes, the tsunami reached common vessel viewing areas (e.g., Glacier View; Fig. 4B), underscoring that hazardous inner-fjord effects can evolve on rapid timescales that limit the value of post-failure alert dissemination. Farther down-fjord, the largest amplification was found in Williams Cove, where the triangular-shaped cove focused tsunami energy four-fold, leading to a runup elevation of 35 m (Fig. 4A), illustrating how fjord geometry and local embayments can strongly modulate runup, a key limitation for simple distance-based hazard rules.

At the mouth of Tracy Arm the wave energy was directed both into Endicott Arm to the south and out into Stephens Passage to the west. However, shallow and irregular bathymetry led to a large reduction in the tsunami height upon exiting Tracy Arm. This can be observed most dramatically near Harbor Island, where the north-facing shorelines experienced tsunami runup greater than 7 m (the location of the kayakers discussed in the Eyewitness Accounts), whereas along south-facing shorelines, less than 1 km away, tsunami runup was less than one meter (Fig. 4B). The maximum tsunami crest elevation in Endicott Arm was near 0.5 m at most locations (Fig. 4D), with localized larger waves in Fords Terror and at the eastern end of Tracy Arm with crest-to-trough tsunami height of 2–2.5 m (refer to the Fords Terror time series in Fig. 4B). Demonstrating both the promise and the limits of far-field observations, such distal records can confirm a landslide-tsunami occurred, but they may not adequately represent the extreme near-field effects.

Like observations from other landslide-tsunamis [e.g., Taan Fiord (*38*)], the spectral transformation of the tsunami from the near-field to the far-field was dramatic. In the immediate near-field, the dominant period of the tsunami was roughly 1 min, which was driven by the time scale of the tsunamigenic phase of the landslide. However, in Juneau, the dominant period of the tsunami was observed and modeled to be 20 min (Fig. 4C). The complex path the tsunami traveled, in addition to the transitions from narrow to wide channels (e.g., Tracy Arm to Stephens Passage) acted as a strong low-pass filter, where low-frequency (long period) wave components traveled with less energy dispersion. This spectral transformation further implies that substantial energy was left behind, or trapped, by geometric and topographic features within the channels. Our numerical simulations, when run for many hours, indicate numerous resonant, or landslide-induced seiche (LIS) modes throughout both Tracy and Endicott arms (e.g., Figs. 4D and 5, A and B, and materials and methods). One of the strongest of these high-order modes existed near a period of 66 s.

Landslide-induced Seiche (LIS)

Emanating from the landslide seismic signal that comprises body waves and surface waves, we observed several monochromatic signals at seismic stations around the world (Figs. 3B and 5, A to D). These signals had periods of 50, 52, 58, 62, 66, and 86 s (Fig. 5B). We focus on the most prominent and long-lasting mode at 66 s, which was observed for up to 36 hours (e.g., at station AK.U33K in Fig. 5A), with a slowly decaying amplitude. Following Svennevig *et al.* (*60*), we investigated the surface wave radiation pattern from radial and transverse waveforms (fig. S11). The data reveal a clear two-lobed radiation pattern (Fig. 5, C and D), with dominant Rayleigh wave energy at stations NNE and SSW of the landslide (e.g., Hawaii, Greenland, Europe), and Love wave energy at stations WNW and ESE (e.g., central North America, Japan). To better quantify the source that produced this radiation pattern, we followed Carrillo-Ponce *et al.* (*61*) by inverting regional 3-component seismic waveforms of the 66 s mode (Fig. 5D) for an oscillating single-force using a resonating source-time function. The best-fit source is a horizontal force oriented ~008–188° with a maximum magnitude of ~2.5 GN (pink arrows in Fig. 5, C to F).

Following Monahan *et al.* (*62*), we leveraged the Surface Water Ocean Topography (SWOT) mission's pixel cloud data (*63*) to assess whether seiche-like structures can be identified within the fjord (refer to supplementary text). SWOT observed clear sea level anomalies in Tracy Arm at 04:28:17 UTC on 11 August, approximately 20 hours after the landslide occurred (Fig. 5E). East of Sawyer Island (Figs. 1 and 5E), considerable noise exists in the data due to the presence of debris and broken ice following the tsunami. Due to inaccuracies in the default pixel cloud flags, we show the raw data to reflect the true noise of the observations. A dominant 7^{th}-order mode (3.5 wavelengths) was observed along the less-noisy 10 km *S*-bend of the fjord, west of Sawyer Island. Our simulated sea-surface height approximately 8 hours after the slide shows a seiche that exhibits the same 7th order, 66 s period mode with the nodes and anti-nodes remaining stable in time (Fig. 5, E and F). The SWOT-observed amplitudes are approximately 15 cm, which is like those observed in the tsunami simulation ~10–15 hours after the slide (refer to

materials and methods for details of the mode identification in the tsunami simulation).

Many of the observed seismic modes have corresponding seiche modes that are predicted by the tsunami (Fig. 5B). For the 66 s period mode, the maximum horizontal water pressure vector of the simulated seiche in the fjord *S*-bend segment has an azimuth of 005°–185°, which matches closely the seismically derived oscillating single-force (008°–188°). Therefore, we infer that the strongest and longest-lasting, 66 s period landslide-induced fjord seiche mode occurred in the fjord *S*-bend, where the tsunami simulation indicates minimal leakage of energy. Aside from the 2023 Dickson Fjord landslide-tsunami event (*60–62*), the 2025 Tracy Arm landslide is the only other known landslide-induced seiche (LIS) generating a days-long, globally observable seismic signal. Many previous, smaller events might have been seismically recorded but not yet discovered. Narrowband seismic monitoring could therefore detect resonant fjord responses even when direct landslide and tsunami observations are unavailable.

The identification of a second days-long, multichromatic LIS indicates that fjords can host persistent, resonant modes that may be preferentially excited by large, nonlinear landslide-tsunamis. Such modes could constitute a fjord-specific harmonic response, or "calling card", detectable seismically even when the landslide itself radiates modest seismic energy. This offers a new pathway for near-real-time detection of hazardous fjord processes in regions with sparse tide-gage data or satellite coverage, motivating automated seismic searches for narrowband signals as part of early-warning frameworks. Long-lived LIS events may also have geomorphic consequences, including sediment depocenters at modal nodes, raising the possibility of identifying paleo-LIS signatures in fjord bathymetry/cores. As warming climates increase the frequency of large landslides in glaciated fjords, LIS events provide a physically grounded link between landslide dynamics, fjord resonance, and emerging seismic and satellite-based monitoring strategies.

Implications

Although no fatalities occurred in the Tracy Arm landslide-tsunami, the event highlights the hazardous nature of tsunamigenic landslides in heavily trafficked coastal areas of polar and sub-polar regions. Here and in similar settings, increased cruise tourism, small-craft traffic, land-based recreation, and expanding infrastructure increases the exposure and thus risk associated with these types of cascading events. The magnitude and far-reaching impacts of the Tracy Arm landslide highlight the benefits of risk mitigation measures including systematic monitoring of unstable slopes, realistic tsunami scenarios, and implementation of practical protective measures for local communities, tourists, and critical infrastructure. A promising area of further investigation could be improved understanding of precursory warning signals either from direct measurement or remote sensing.

Materials and methods are available in the supplementary materials.

REFERENCES AND NOTES

1. D. J. Miller, The Alaska earthquake of July 10, 1958: Giant wave in Lituya Bay. *Bull. Seismol. Soc. Am.* **50**, 253–266 (1960). doi:10.1785/BSSA0500020253
2. H. Fritz, F. Mohammed, J. Yoo, Lituya Bay landslide impact generated mega-tsunami 50th Anniversary. *Pure Appl. Geophys.* **166**, 153–175 (2009). doi:10.1007/s00024-008-0435-4
3. İ. Ç. Kolçak, O. Çetin, M. Saka, Environmental impact of cruise shipping in Arctic region. *Int. J. Environ. Geoinformatics* **9**, 1–10 (2022). doi:10.30897/ijegeo.957262
4. Cruise Line International Association, History of cruise industry in Alaska; https://akcruise.org/economy/alaska-cruise-history/.
5. S. Colt, S. Martin, J. Mieren, M. Tomeo, "Recreation and tourism in south-central Alaska: Patterns and prospects" (Gen. Tech. Rep. PNW-GTR-551, US Department of Agriculture, Forest Service, Pacific Northwest Research Station, 2002).
6. M. Aanesen, J. Falk-Andersson, G. K. Vondolia, T. Borch, S. Navrud, D. Tinch, Valuing coastal recreation and the visual intrusion from commercial activities in Arctic Norway. *Ocean Coast. Manage.* **153**, 157–167 (2018). doi:10.1016/j.ocecoaman.2017.12.017
7. W. D. Smith, S. A. Dunning, N. Ross, J. Telling, E. K. Jensen, D. H. Shugar, J. A. Coe, M. Geertsema, Revising supraglacial rock avalanche magnitudes and frequencies in Glacier Bay National Park, Alaska. *Geomorphology* **425**, 108591 (2023). doi:10.1016/j.geomorph.2023.108591
8. B. Davies, R. McNabb, J. Bendle, J. Carrivick, J. Ely, T. Holt, B. Markle, C. McNeil, L. Nicholson, M. Pelto, Accelerating glacier volume loss on Juneau Icefield driven by hypsometry and melt-accelerating feedbacks. *Nat. Commun.* **15**, 5099 (2024). doi:10.1038/s41467-024-49269-y Medline
9. J. Kavan, M. Szczypińska, W. Kochtitzky, L. Farquharson, M. Bendixen, M. C. Strzelecki, New coasts emerging from the retreat of Northern Hemisphere marine-terminating glaciers in the twenty-first century. *Nat. Clim. Chang.* **15**, 528–537 (2025). doi:10.1038/s41558-025-02282-5
10. K. Svennevig, M. Keiding, N. J. Korsgaard, A. Lucas, M. Owen, M. D. Poulsen, J. Priebe, E. V. Sørensen, C. Morino, Uncovering a 70-year-old permafrost degradation induced disaster in the Arctic, the 1952 Niiortuut landslide-tsunami in central West Greenland. *Sci. Total Environ.* **859**, 160110 (2023). doi:10.1016/j.scitotenv.2022.160110 Medline
11. K. Svennevig, M. Keiding, E. V. Sørensen, F. Løvholt, S. Glimsdal, L. F. Perez, M. J. Owen, C. Morino, Two similar permafrost degradation landslides at Paatuut, West Greenland, caused tsunamis of substantially different magnitudes. *Landslides* **22**, 1455–1474 (2025). doi:10.1007/s10346-024-02439-x
12. P. Saemundsson, C. Morino, S. J. Conway, "5.22 - Mass-movements in cold and polar climates" in *Treatise on Geomorphology*, J. F. Shroder, Ed. (Academic Press, ed. 2, 2022), pp. 350–370.
13. K. Svennevig, T. Dahl-Jensen, M. Keiding, J. P. Merryman Boncori, T. B. Larsen, S. Salehi, A. Munck Solgaard, P. H. Voss, Evolution of events before and after the 17 June 2017 rock avalanche at Karrat Fjord, West Greenland – a multidisciplinary approach to detecting and locating unstable rock slopes in a remote Arctic area. *Earth Surf. Dyn.* **8**, 1021–1038 (2020). doi:10.5194/esurf-8-1021-2020
14. S. Matti, M. Cullen, U. Reichardt, A. Vigfúsdóttir, Planned relocation due to landslide-triggered tsunami risk in recently deglaciated areas. *Int. J. Disaster Risk Reduct.* **86**, 103536 (2023). doi:10.1016/j.ijdrr.2023.103536
15. Nuka Research and Planning Group, LLC, "Tsunami hazards guidance for vessel operators: Workshop summary" (2024); https://www.pwsrcac.org/wp-content/uploads/Tsunami-Hazards-Guidance-for-Vessel-Operators-Workshop-Summary.pdf.
16. M. M. Miller, Inventory of terminal position changes in Alaskan coastal glaciers since the 1750's. *Proc. Am. Philos. Soc.* **108**, 257–273 (1964).
17. F. H. Wilson, C. P. Hults, C. G. Mull, S. M. Karl, Geologic map of Alaska (2015);

https://pubs.usgs.gov/publication/sim3340.
18. D. A. Brew, D. Grybeck, USGS B 1525 - Geology of the Tracy Arm-Fords Terror Wilderness Study Area and vicinity, Alaska (1984); https://dggs.alaska.gov/pubs/id/4582.
19. USGS, Modeled probabilistic map of near-surface permafrost within Alaska; https://www.usgs.gov/media/images/modeled-probabilistic-map-near-surface-permafrost-within-alaska.
20. S. Gruber, Derivation and analysis of a high-resolution estimate of global permafrost zonation. *Cryosphere* **6**, 221–233 (2012). doi:10.5194/tc-6-221-2012
21. J. H. Mercer, The response of fjord glaciers to changes in the firn limit. *J. Glaciol.* **3**, 850–858 (1961). doi:10.3189/S0022143000027222
22. A. K. Melkonian, M. J. Willis, M. E. Pritchard, Stikine Icefield mass loss between 2000 and 2013/2014. *Front. Earth Sci.* **4**, 89 (2016). doi:10.3389/feart.2016.00089
23. E. Berthier, C. Larsen, W. J. Durkin, M. J. Willis, M. E. Pritchard, Brief communication: Unabated wastage of the Juneau and Stikine icefields (southeast Alaska) in the early 21st century. *Cryosphere* **12**, 1523–1530 (2018). doi:10.5194/tc-12-1523-2018
24. R. Hugonnet, R. McNabb, E. Berthier, B. Menounos, C. Nuth, L. Girod, D. Farinotti, M. Huss, I. Dussaillant, F. Brun, A. Kääb, Accelerated global glacier mass loss in the early twenty-first century. *Nature* **592**, 726–731 (2021). doi:10.1038/s41586-021-03436-z Medline
25. M. S. Pelto, Mass balance of south-east Alaska and north-west British Columbia glaciers from 1976 to 1984: Methods and results. *Ann. Glaciol.* **9**, 189–194 (1987). doi:10.3189/S0260305500000598
26. L. Zeller, D. McGrath, L. Sass, C. E. Florentine, J. Z. Downs, Annual end-of-summer snow cover on glaciers in Alaska and northwest Canada. US Geological Survey (2024); https://doi.org/10.5066/P1QHST6F.
27. L. Zeller, D. McGrath, L. Sass, C. Florentine, J. Downs, Equilibrium line altitudes, accumulation areas and the vulnerability of glaciers in Alaska. *J. Glaciol.* **71**, e28 (2025). doi:10.1017/jog.2024.65
28. Marine Exchange of Alaska, Vessel traffic in Tracy Arm – Ford's Terror Wilderness; https://www.mxak.org/.
29. O. Hungr, S. Leroueil, L. Picarelli, The Varnes classification of landslide types, an update. *Landslides* **11**, 167–194 (2014). doi:10.1007/s10346-013-0436-y
30. D. M. Cruden, D. Varnes, "Landslide types and processes" in *Landslides Investigation and Mitigation*, A. K. Turner, R. L. Schuster, Eds. (Transportation Research Board, 1996), pp. 36–75.
31. C. Read, J. Lyons, E. Stephani, D. Staley, Oblique aerial photography and videography of the August 10, 2025 Tracy Arm landslide and tsunami, southeast Alaska. US Geological Survey (2025): https://doi.org/10.5066/P14SPXJG.
32. W. Kochtitzky, L. Copland, Retreat of northern hemisphere marine-terminating glaciers, 2000–2020. *Geophys. Res. Lett.* **49**, e2021GL096501 (2022). doi:10.1029/2021GL096501
33. National Oceanic and Atmospheric Administration, Alaska Part 6, 1898, Coast Survey's Historical Map and Chart Collection; https://historicalcharts.noaa.gov/#map.
34. C. F. Larsen, R. J. Motyka, A. A. Arendt, K. A. Echelmeyer, P. E. Geissler, Glacier changes in southeast Alaska and northwest British Columbia and contribution to sea level rise. *J. Geophys. Res.* **112**, F01007 (2007). doi:10.1029/2006JF000586
35. C. Porter, I. Howat, M.-J. Noh, E. Husby, S. Khuvis, E. Danish, K. Tomko, J. Gardiner, A. Negrete, B. Yadav, J. Klassen, C. Kelleher, M. Cloutier, J. Bakker, J. Enos, G. Arnold, G. Bauer, P. Morin, ArcticDEM - Strips, Version 4.1. Harvard Dataverse (2022); https://doi.org/10.7910/DVN/C98DVS.
36. J. Walden, M. Jacquemart, B. Higman, R. Hugonnet, A. Manconi, D. Farinotti, Landslide activation during deglaciation in a fjord-dominated landscape: Observations from southern Alaska (1984–2022). *Nat. Hazards Earth Syst. Sci.* **25**, 2045–2073 (2025). doi:10.5194/nhess-25-2045-2025
37. E. Lemaire, A. Dufresne, P. Hamdi, B. Higman, G. J. Wolken, F. Amann, Back-analysis of the paraglacial slope failure at Grewingk Glacier and Lake, Alaska. *Landslides* **21**, 775–789 (2024). doi:10.1007/s10346-023-02177-6
38. B. Higman, D. H. Shugar, C. P. Stark, G. Ekström, M. N. Koppes, P. Lynett, A. Dufresne, P. J. Haeussler, M. Geertsema, S. Gulick, A. Mattox, J. G. Venditti, M. A. L. Walton, N. McCall, E. Mckittrick, B. MacInnes, E. L. Bilderback, H. Tang, M. J. Willis, B. Richmond, R. S. Reece, C. Larsen, B. Olson, J. Capra, A. Ayca, C. Bloom, H. Williams, D. Bonno, R. Weiss, A. Keen, V. Skanavis, M. Loso, The 2015 landslide and tsunami in Taan Fiord, Alaska. *Sci. Rep.* **8**, 12993 (2018). doi:10.1038/s41598-018-30475-w Medline
39. M. Geertsema, B. Menounos, G. Bullard, J. L. Carrivick, J. J. Clague, C. Dai, D. Donati, G. Ekström, J. M. Jackson, P. Lynett, M. Pichierri, A. Pon, D. H. Shugar, D. Stead, J. Del Bel Belluz, P. Friele, I. Giesbrecht, D. Heathfield, T. Millard, S. Nasonova, A. J. Schaeffer, B. C. Ward, D. Blaney, E. Blaney, C. Brillon, C. Bunn, W. Floyd, B. Higman, K. E. Hughes, W. McInnes, K. Mukherjee, M. A. Sharp, The 28 November 2020 landslide, tsunami, and outburst flood – a hazard cascade associated with rapid deglaciation at Elliot Creek, British Columbia, Canada. *Geophys. Res. Lett.* **49**, e2021GL096716 (2022). doi:10.1029/2021GL096716
40. E. Karasözen, M. E. West, K. R. Barnhart, J. J. Lyons, T. Nichols, L. N. Schaefer, B. Bahng, S. Ohlendorf, D. M. Staley, G. J. Wolken, 2024 Surprise Inlet landslides: Insight from a prototype landslide-triggered tsunami monitoring system in Prince William Sound, Alaska. *Geophys. Res. Lett.* **52**, e2025GL115911 (2025). doi:10.1029/2025GL115911
41. L. L. Pedersen, K. Svennevig, C. Morino, A. S. Søndergaard, C. Pearce, L. F. Pérez, A. Damsgaard, J. Olsen, M. F. Knudsen, A. Noblet, N. K. Larsen, A giant Early Holocene tsunamigenic rock-ice avalanche in South Greenland preconditioned by glacial debuttressing. *Geomorphology* **492**, 110057 (2026). doi:10.1016/j.geomorph.2025.110057
42. Alaska Ocean Observing System (AOOS), Ocean Data Explorer, Ocean Data Explorer; https://portal.aoos.org/#map.
43. Synoptic, Synoptic Data Viewer; https://synopticdata.com/data-viewer/.
44. R. N. Ing, J. C. Ely, J. M. Jones, B. J. Davies, Surface mass balance modelling of the Juneau Icefield highlights the potential for rapid ice loss by the mid-21st century. *J. Glaciol.* **71**, e11 (2025). doi:10.1017/jog.2024.82
45. M. Berdahl, J. Christian, E. Steig, G. Roe, "Adapting temperature-attribution methodologies to understand industrial-era glacier retreat (EGU25-20608)" (2025); https://meetingorganizer.copernicus.org/EGU25/EGU25-20608.html.
46. Intergovernmental Panel on Climate Change (IPCC), "Summary for policymakers" in *Climate Change 2021: The Physical Science Basis. Contribution of Working Group I to the Sixth Assessment Report of the Intergovernmental Panel on Climate Change*, V. Masson-Delmotte, P. Zhai, A. Pirani, S. L. Connors, C. Péan, S. Berger, N. Caud, Y. Chen, L. Goldfarb, M. I. Gomis, M. Huang, K. Leitzell, E. Lonnoy, J. B. R. Matthews, T. K. Maycock, T. Waterfield, O. Yelekçi, R. Yu, B. Zhou, Eds. (IPCC, 2021).
47. K. Haustein, F. E. L. Otto, V. Venema, P. Jacobs, K. Cowtan, Z. Hausfather, R. G. Way, B. White, A. Subramanian, A. P. Schurer, A limited role for unforced internal variability in Twentieth-century warming. *J. Clim.* **32**, 4893–4917 (2019). doi:10.1175/JCLI-D-18-0555.1
48. C. Huggel, J. Caplan-Auerbach, C. F. Waythomas, R. L. Wessels, Monitoring and modeling ice-rock avalanches from ice-capped volcanoes: A case study of frequent large avalanches on Iliamna Volcano, Alaska. *J. Volcanol. Geotherm. Res.* **168**, 114–136 (2007). doi:10.1016/j.jvolgeores.2007.08.009
49. J. Caplan-Auerbach, C. Huggel, Precursory seismicity associated with frequent, large ice avalanches on Iliamna volcano, Alaska, USA. *J. Glaciol.* **53**, 128–140 (2007). doi:10.3189/172756507781833866
50. M. Yamada, J. Mori, Y. Matsushi, Possible stick-slip behavior before the Rausu landslide inferred from repeating seismic events. *Geophys. Res. Lett.* **43**, 9038–9044 (2016). doi:10.1002/2016GL069288
51. P. Poli, Creep and slip: Seismic precursors to the Nuugaatsiaq landslide (Greenland). *Geophys. Res. Lett.* **44**, 8832–8836 (2017). doi:10.1002/2017GL075039
52. G. Ekström, Global detection and location of seismic sources by using surface waves. *Bull. Seismol. Soc. Am.* **96**, 1201–1212 (2006). doi:10.1785/0120050175
53. E. Karasözen, M. E. West, Toward the rapid seismic assessment of landslides in coastal Alaska. *Seismic Record* **4**, 43–51 (2024). doi:10.1785/0320230044
54. D. Fee, L. Toney, K. Kim, R. W. Sanderson, A. M. Iezzi, R. S. Matoza, S. De Angelis, A. D. Jolly, J. L. Lyons, M. M. Haney, Local explosion detection and infrasound localization by reverse time migration using 3-D finite-difference wave propagation. *Front. Earth Sci. (Lausanne)* **9**, 620813 (2021). doi:10.3389/feart.2021.620813
55. E. Stone, "'Pure chaos out of nowhere': Mega-landslide and tsunami rip through Tracy Arm south of Juneau," *Alaska Public Media*, 12 August 2025;

https://alaskapublic.org/news/environment/2025-08-12/pure-chaos-out-of-nowhere-mega-landslide-and-tsunami-rip-through-tracy-arm-south-of-juneau.
56. C. K. Bloom, B. MacInnes, B. Higman, D. H. Shugar, J. G. Venditti, B. M. Richmond, E. L. Bilderback, Catastrophic landscape modification from a massive landslide tsunami in Taan Fiord, Alaska. *Geomorphology* **353**, 107029 (2020). doi:10.1016/j.geomorph.2019.107029
57. S. N. Ward, S. Day, The 1958 Lituya Bay landslide and tsunami — A tsunami ball approach. *J. Earthq. Tsunami* **4**, 285–319 (2010). doi:10.1142/S1793431110000893
58. S. Tavakkol, P. Lynett, Celeris: A GPU-accelerated open source software with a Boussinesq-type wave solver for real-time interactive simulation and visualization. *Comput. Phys. Commun.* **217**, 117–127 (2017). doi:10.1016/j.cpc.2017.03.002
59. S. Tavakkol, P. Lynett, Celeris Base: An interactive and immersive Boussinesq-type nearshore wave simulation software. *Comput. Phys. Commun.* **248**, 106966 (2020). doi:10.1016/j.cpc.2019.106966
60. K. Svennevig, S. P. Hicks, T. Forbriger, T. Lecocq, R. Widmer-Schnidrig, A. Mangeney, C. Hibert, N. J. Korsgaard, A. Lucas, C. Satriano, R. E. Anthony, A. Mordret, S. Schippkus, S. Rysgaard, W. Boone, S. J. Gibbons, K. L. Cook, S. Glimsdal, F. Løvholt, K. Van Noten, J. D. Assink, A. Marboeuf, A. Lomax, K. Vanneste, T. Taira, M. Spagnolo, R. De Plaen, P. Koelemeijer, C. Ebeling, A. Cannata, W. D. Harcourt, D. G. Cornwell, C. Caudron, P. Poli, P. Bernard, E. Larose, E. Stutzmann, P. H. Voss, B. Lund, F. Cannavo, M. J. Castro-Díaz, E. Chaves, T. Dahl-Jensen, N. Pinho Dias, A. Déprez, R. Develter, D. Dreger, L. G. Evers, E. D. Fernández-Nieto, A. M. G. Ferreira, G. Funning, A.-A. Gabriel, M. Hendrickx, A. L. Kafka, M. Keiding, J. Kerby, S. A. Khan, A. K. Dideriksen, O. D. Lamb, T. B. Larsen, B. Lipovsky, I. Magdalena, J.-P. Malet, M. Myrup, L. Rivera, E. Ruiz-Castillo, S. Wetter, B. Wirtz, A rockslide-generated tsunami in a Greenland fjord rang Earth for 9 days. *Science* **385**, 1196–1205 (2024). doi:10.1126/science.adm9247 Medline
61. A. Carrillo-Ponce, S. Heimann, G. M. Petersen, T. R. Walter, S. Cesca, T. Dahm, The 16 September 2023 Greenland megatsunami: Analysis and modeling of the source and a week-long, monochromatic seismic signal. *The Seismic Record* **4**, 172–183 (2024). doi:10.1785/0320240013
62. T. Monahan, T. Tang, S. Roberts, T. A. A. Adcock, Observations of the seiche that shook the world. *Nat. Commun.* **16**, 4777 (2025). doi:10.1038/s41467-025-59851-7 Medline
63. Surface Water Ocean Topography (SWOT), SWOT Level 2 Water Mask Pixel Cloud Data Product, Version D. Physical Oceanography Distributed Active Archive Center (PO.DAAC) (2025); https://podaac.jpl.nasa.gov/dataset/SWOT_L2_HR_PIXC_D.
64. R. G. I. Consortium, Randolph Glacier Inventory - A Dataset of Global Glacier Outlines. (NSIDC-0770, Version 6). National Snow and Ice Data Center (2017); https://doi.org/10.7265/4m1f-gd79.
65. Alaska Earthquake Center, AK; Alaska Geophysical Network. International Federation of Digital Seismograph Networks (1987); https://doi.org/10.7914/SN/AK.
66. Natural Resources Canada, CN: Canadian National Seismograph Network. International Federation of Digital Seismograph Networks (1975); https://doi.org/10.7914/SN/CN.
67. GEUS Geological Survey of Denmark and Greenland, DK: Danish Seismological Network. International Federation of Digital Seismograph Networks (1976); https://doi.org/10.7914/NW3X-DF02.
68. Geoscope, GEOSCOPE Network; http://geoscope.ipgp.fr/networks/detail/G/.
69. GEOFON Data Centre, GEOFON Seismic Network. GFZ Data Services (1993); https://doi.org/10.14470/TR560404.
70. Scripps Institution of Oceanography, Global Seismograph Network - IRIS/IDA. International Federation of Digital Seismograph Networks (1986); https://doi.org/10.7914/SN/II.
71. Albuquerque Seismological Laboratory/USGS, Global Seismograph Network, (GSN - IRIS/USGS). International Federation of Digital Seismograph Networks (1988); https://doi.org/10.7914/SN/IU.
72. Albuquerque Seismological Laboratory (ASL)/USGS, US: United States National Seismic Network. International Federation of Digital Seismograph Networks (1990); https://doi.org/10.7914/SN/US.
73. US Geological Survey, EarthExplorer; https://earthexplorer.usgs.gov/.
74. European Space Agency, Copernicus Browser; https://browser.dataspace.copernicus.eu/.
75. A. Fathian, D. Shugar, SkySatPrep. Zenodo (2025); https://doi.org/10.5281/zenodo.17156720.
76. A. Fathian, D. Shugar, demalign. Zenodo (2025); https://doi.org/10.5281/zenodo.17158093.
77. National Oceanic and Atmospheric Administration, Tide predictions – NOAA tides and currents; https://tidesandcurrents.noaa.gov/tide_predictions.html.
78. D. H. Shugar, Shugar et al Tracy Arm supplementary files. Zenodo (2026); https://doi.org/10.5281/zenodo.18306727.
79. Berkeley Earth, Data overview; https://berkeleyearth.org/data/.
80. R. C. Gonzalez, R. E. Woods, *Digital Image Processing* (Pearson Education, ed. 4, 2018).
81. Y. Chang, C. Jung, P. Ke, H. Song, J. Hwang, Automatic contrast-limited adaptive histogram equalization with dual gamma correction. *IEEE Access* **6**, 11782–11792 (2018). doi:10.1109/ACCESS.2018.2797872
82. K. Zuiderveld, "Contrast limited adaptive histogram equalization" in *Graphics Gems IV*, P. S. Heckbert, Ed. (Academic Press, 1994), pp. 474–485.
83. E. Rouault, F. Warmerdam, K. Schwehr, A. Kiselev, H. Butler, M. Łoskot, T. Szekeres, E. Tourigny, M. Landa, I. Miara, B. Elliston, K. Chaitanya, L. Plesea, D. Morissette, A. Jolma, N. Dawson, D. Baston, C. de Stigter, H. Miura, GDAL, version v3.11.4. Zenodo (2025); https://doi.org/10.5281/zenodo.5884351.
84. J.-S. R. Over, A. C. Ritchie, C. J. Kranenburg, J. A. Brown, D. D. Buscombe, T. Noble, C. R. Sherwood, J. A. Warrick, P. A. Wernette, "Processing Coastal Imagery With Agisoft Metashape Professional Edition, Version 1.6—Structure From Motion Workflow Documentation" (Open-File Report 2021–1039, US Geological Survey, 2021).
85. E. Rupnik, M. Daakir, M. Pierrot Deseilligny, MicMac – a free, open-source solution for photogrammetry. *Open Geospatial Data Softw. Stand.* **2**, 14 (2017). doi:10.1186/s40965-017-0027-2
86. E. Rupnik, M. Pierrot-Deseilligny, A. Delorme, 3D reconstruction from multi-view VHR-satellite images in MicMac. *ISPRS J. Photogramm. Remote Sens.* **139**, 201–211 (2018). doi:10.1016/j.isprsjprs.2018.03.016
87. J. Grodecki, G. Dial, Block adjustment of high-resolution satellite images described by rational polynomials. *Photogramm. Eng. Remote Sensing* **69**, 59–68 (2003). doi:10.14358/PERS.69.1.59
88. G. Kuschk, P. d'Angelo, D. Gaudrie, P. Reinartz, D. Cremers, Spatially regularized fusion of multiresolution digital surface models. *IEEE Trans. Geosci. Remote Sens.* **55**, 1477–1488 (2017). doi:10.1109/TGRS.2016.2625040
89. D. E. Shean, O. Alexandrov, Z. M. Moratto, B. E. Smith, I. R. Joughin, C. Porter, P. Morin, An automated, open-source pipeline for mass production of digital elevation models (DEMs) from very-high-resolution commercial stereo satellite imagery. *ISPRS J. Photogramm. Remote Sens.* **116**, 101–117 (2016). doi:10.1016/j.isprsjprs.2016.03.012
90. R. A. Beyer, O. Alexandrov, S. McMichael, The Ames Stereo Pipeline: NASA's open source software for deriving and processing terrain data. *Earth Space Sci.* **5**, 537–548 (2018). doi:10.1029/2018EA000409
91. C. Nuth, A. Kääb, Co-registration and bias corrections of satellite elevation data sets for quantifying glacier thickness change. *Cryosphere* **5**, 271–290 (2011). doi:10.5194/tc-5-271-2011
92. F. Pomerleau, F. Colas, R. Siegwart, S. Magnenat, Comparing ICP variants on real-world data sets. *Auton. Robots* **34**, 133–148 (2013). doi:10.1007/s10514-013-9327-2
93. Copernicus Data Space Ecosystem, Copernicus DEM - Global and European Digital Elevation Mode; https://dataspace.copernicus.eu/explore-data/data-collections/copernicus-contributing-missions/collections-description/COP-DEM.
94. P. Bailey, J. Wheaton, M. Reimer, J. Brasington, Geomorphic Change Detection Software, Version 7.5.0. Zenodo (2020); https://doi.org/10.5281/zenodo.7248344.
95. J. M. Wheaton, J. Brasington, S. E. Darby, D. A. Sear, Accounting for uncertainty in DEMs from repeat topographic surveys: Improved sediment budgets. *Earth Surf. Process. Landf.* **35**, 136–156 (2010). doi:10.1002/esp.1886
96. S. N. Lane, R. M. Westaway, D. Murray Hicks, Estimation of erosion and deposition

volumes in a large, gravel-bed, braided river using synoptic remote sensing. *Earth Surf. Process. Landf.* **28**, 249–271 (2003). doi:10.1002/esp.483
97. A. Fathian, StereonetForge, Version v0.2.1. Zenodo (2025); https://doi.org/10.5281/zenodo.17140123.
98. P. J. Lynett, R. Weiss, B. M. Higman, A. F. Mattox, A. S. Keen, V. Skanavis, H. Tang, A. Ayca, N. Kalligeris, Tsunami runup survey data from the Taan Fjord landslide event. *Sci. Data* **12**, 1341 (2025). doi:10.1038/s41597-025-05617-1 Medline
99. R. A. Rohde, Z. Hausfather, The Berkeley Earth land/ocean temperature record. *Earth Syst. Sci. Data* **12**, 3469–3479 (2020). doi:10.5194/essd-12-3469-2020
100. K. E. Taylor, R. J. Stouffer, G. A. Meehl, An overview of CMIP5 and the experiment design. *Bull. Am. Meteorol. Soc.* **93**, 485–498 (2012). doi:10.1175/BAMS-D-11-00094.1
101. V. Eyring, S. Bony, G. A. Meehl, C. A. Senior, B. Stevens, R. J. Stouffer, K. E. Taylor, Overview of the Coupled Model Intercomparison Project Phase 6 (CMIP6) experimental design and organization. *Geosci. Model Dev.* **9**, 1937–1958 (2016). doi:10.5194/gmd-9-1937-2016
102. A. A. Arendt, K. A. Echelmeyer, W. D. Harrison, C. S. Lingle, V. B. Valentine, Rapid wastage of Alaska glaciers and their contribution to rising sea level. *Science* **297**, 382–386 (2002). doi:10.1126/science.1072497 Medline
103. E. Berthier, E. Schiefer, G. K. C. Clarke, B. Menounos, F. Remy, Contribution of Alaskan glaciers to sea-level rise derived from satellite imagery. *Nat. Geosci.* **3**, 92–95 (2010). doi:10.1038/ngeo737
104. R. W. McNabb, R. Hock, Alaska tidewater glacier terminus positions, 1948-2012. *J. Geophys. Res. Earth Surf.* **119**, 153–167 (2014). doi:10.1002/2013JF002915
105. M. Van Wyk de Vries, K. Arrell, G. K. Basyal, A. L. Densmore, A. Dunant, E. L. Harvey, G. K. Jimee, M. E. Kincey, S. Li, D. Singh Pujara, R. Shrestha, N. J. Rosser, S. J. Dadson, Detection of slow-moving landslides through automated monitoring of surface deformation using Sentinel-2 satellite imagery. *Earth Surf. Process. Landf.* **49**, 1397–1410 (2024). doi:10.1002/esp.5775
106. M. Van Wyk de Vries, A. D. Wickert, Glacier Image Velocimetry: An open-source toolbox for easy and rapid calculation of high-resolution glacier velocity fields. *Cryosphere* **15**, 2115–2132 (2021). doi:10.5194/tc-15-2115-2021
107. D. Massonnet, M. Rossi, C. Carmona, F. Adragna, G. Peltzer, K. Feigl, T. Rabaute, The displacement field of the Landers earthquake mapped by radar interferometry. *Nature* **364**, 138–142 (1993). doi:10.1038/364138a0
108. D. Sandwell, R. Mellors, X. Tong, M. Wei, P. Wessel, Open radar interferometry software for mapping surface Deformation. *Eos* **92**, 234 (2011). doi:10.1029/2011EO280002
109. J.-F. Jans, E. Beernaert, M. De Breuck, I. Brangers, D. Dunmire, G. De Lannoy, H. Lievens, Sensitivity of Sentinel-1 C-band SAR backscatter, polarimetry and interferometry to snow accumulation in the Alps. *Remote Sens. Environ.* **316**, 114477 (2025). doi:10.1016/j.rse.2024.114477
110. R. Torres, P. Snoeij, D. Geudtner, D. Bibby, M. Davidson, E. Attema, P. Potin, B. Rommen, N. Floury, M. Brown, I. N. Traver, P. Deghaye, B. Duesmann, B. Rosich, N. Miranda, C. Bruno, M. L'Abbate, R. Croci, A. Pietropaolo, M. Huchler, F. Rostan, GMES Sentinel-1 mission. *Remote Sens. Environ.* **120**, 9–24 (2012). doi:10.1016/j.rse.2011.05.028
111. NASA/JPL/OPERA, OPERA Surface Displacement from Sentinel-1 validated product (Version 1). NASA EarthData (2025); https://doi.org/10.5067/SNWG/OPL3DISPS1-V1.
112. K. T. Walker, M. A. H. Hedlin, C. de Groot-Hedlin, J. Vergoz, A. Le Pichon, D. P. Drob, Source location of the 19 February 2008 Oregon bolide using seismic networks and infrasound arrays. *J. Geophys. Res. Solid Earth* **115**, B12329 (2010). doi:10.1029/2010JB007863
113. R. W. Sanderson, R. S. Matoza, D. Fee, M. M. Haney, J. J. Lyons, Remote detection and location of explosive volcanism in Alaska with the EarthScope Transportable Array. *J. Geophys. Res. Solid Earth* **125**, e2019JB018347 (2020). doi:10.1029/2019JB018347
114. G. Ekström, C. P. Stark, Simple scaling of catastrophic landslide dynamics. *Science* **339**, 1416–1419 (2013). doi:10.1126/science.1232887 Medline
115. C. Hibert, G. Ekström, C. P. Stark, Dynamics of the Bingham Canyon Mine landslides from seismic signal analysis. *Geophys. Res. Lett.* **41**, 4535–4541 (2014). doi:10.1002/2014GL060592
116. R. J. Caldwell, L. A. Taylor, B. W. Eakins, K. S. Carignan, S. V. Collins, "Digital Elevation Models of Juneau and Southeast Alaska: Procedures, Data Sources and Analysis" (NOAA Technical Memorandum NGDC-53, National Oceanographic and Atmospheric Administration, 2012); https://repository.library.noaa.gov/view/noaa/4275.
117. US Geological Survey, 5 Meter Alaska Digital Elevation Models (DEMs) - USGS National Map 3DEP Downloadable Data Collection - ScienceBase-Catalog (2022); https://www.sciencebase.gov/catalog/item/5641fe98e4b0831b7d62e758.
118. National Oceanic and Atmospheric Administration, Report for H11759 (2007); https://www.ngdc.noaa.gov/nos/H10001-H12000/H11759.html.
119. National Oceanic and Atmospheric Administration, Report for H11760 (2007); https://www.ngdc.noaa.gov/nos/H10001-H12000/H11760.html.
120. National Oceanic and Atmospheric Administration, Report for H11998 (2008); https://www.ngdc.noaa.gov/nos/H10001-H12000/H11998.html.
121. National Oceanic and Atmospheric Administration, Report for H13006 (2018); https://www.ngdc.noaa.gov/nos/H12001-H14000/H13006.html.
122. National Oceanic and Atmospheric Administration, Report for H13007 (2018); https://www.ngdc.noaa.gov/nos/H12001-H14000/H13007.html.
123. National Oceanic and Atmospheric Administration, Report for F00811 (2020); https://www.ngdc.noaa.gov/nos/F00001-F02000/F00811.html.
124. National Oceanic and Atmospheric Administration, Report for F00833 (2021); https://www.ngdc.noaa.gov/nos/F00001-F02000/F00833.html.
125. P. A. Madsen, R. Murray, O. R. Sørensen, A new form of the Boussinesq equations with improved linear dispersion characteristics. *Coast. Eng.* **15**, 371–388 (1991). doi:10.1016/0378-3839(91)90017-B
126. N. Kalligeris, Y. Kim, P. J. Lynett, Wave-induced shallow-water monopolar vortex: Large-scale experiments. *J. Fluid Mech.* **910**, A17 (2021). doi:10.1017/jfm.2020.980
127. National Oceanic and Atmospheric Administration, Climate Data Online Search (2025); https://www.ncdc.noaa.gov/cdo-web/search.
128. US Department of Agriculture, Natural Resources Conservation Service, Long Lake, Site Information and Reports, Site 1001 (2025); https://wcc.sc.egov.usda.gov/nwcc/site?sitenum=1001.
129. D. Nash, J. J. Rutz, A. Jacobs, Atmospheric rivers in Southeast Alaska: Meteorological conditions associated with extreme precipitation. *J. Geophys. Res. Atmos.* **129**, e2023JD039294 (2024). doi:10.1029/2023JD039294
130. National Geophysical Data Center/World Data Service, NCEI/WDS Global Historical Tsunami Database, 2100 BC to Present. National Centers for Environmental Information; https://doi.org/10.7289/V5PN93H7.
131. N. Waldmann, K. Vasskog, G. Simpson, E. Chapron, E. W. N. Støren, L. Hansen, J.-L. Loizeau, A. Nesje, D. Ariztegui, Anatomy of a catastrophe: Reconstructing the 1936 rock fall and tsunami event in Lake Lovatnet, western Norway. *Front. Earth Sci.* **9**, 671378 (2021). doi:10.3389/feart.2021.671378
132. S. G. Evans, The 1946 Mount Colonel Foster rock avalanche and associated displacement wave, Vancouver Island, British Columbia. *Can. Geotech. J.* **26**, 447–452 (1989). doi:10.1139/t89-057
133. S. Bosa, M. Petti, Shallow water numerical model of the wave generated by the Vajont landslide. *Environ. Model. Softw.* **26**, 406–418 (2011). doi:10.1016/j.envsoft.2010.10.001
134. T. Parsons, E. L. Geist, H. F. Ryan, H. J. Lee, P. J. Haeussler, P. Lynett, P. E. Hart, R. Sliter, E. Roland, Source and progression of a submarine landslide and tsunami: The 1964 Great Alaska earthquake at Valdez. *J. Geophys. Res. Solid Earth* **119**, 8502–8516 (2014). doi:10.1002/2014JB011514
135. S. F. L. Watt, D. M. Pyle, J. A. Naranjo, T. A. Mather, Landslide and tsunami hazard at Yate volcano, Chile as an example of edifice destruction on strike-slip fault zones. *Bull. Volcanol.* **71**, 559–574 (2009). doi:10.1007/s00445-008-0242-x
136. G. Kjartansson, The Steinsholtshlaup, central-south Iceland on January 15th, 1967. *Jokull* **17**, 249–262 (1967).
137. G. C. Wiles, P. E. Calkin, Reconstruction of a debris-slide-initiated flood in the southern Kenai Mountains, Alaska. *Geomorphology* **5**, 535–546 (1992). doi:10.1016/0169-555X(92)90024-I
138. C. L. Rosenfeld, Observations on the Mount St. Helens Eruption. *Am. Sci.* **68**, 494–509 (1980).
139. T. Toulkeridis, I. Sinde-González, O. Jheny, Glacial lake tsunami of 13 October 2000 on "El Altar" volcano of Ecuador. *Sci. Tsunami Hazards* **41**, 311 (2022).
140. J. Wang, L. Xiao, S. N. Ward, J. Du, Tsunami Squares modeling of the 2007 Dayantang landslide generated waves considering the effects in slide/water

interactions. *Eng. Geol.* **284**, 106032 (2021). doi:10.1016/j.enggeo.2021.106032
141. A. Schöpa, W.-A. Chao, B. P. Lipovsky, N. Hovius, R. S. White, R. G. Green, J. M. Turowski, Dynamics of the Askja caldera July 2014 landslide, Iceland, from seismic signal analysis: Precursor, motion and aftermath. *Earth Surf. Dyn.* **6**, 467–485 (2018). doi:10.5194/esurf-6-467-2018
142. H. M. Fritz, T. Giachetti, S. A. Anderson, D. Gauthier, "Field Survey of the 17 June 2017 Landslide generated Tsunami in Karrat Fjord, Greenland" (2018); https://ui.adsabs.harvard.edu/abs/2017AGUFMNH12A..01F/abstract.
143. V. Gusiakov, A. Makhinov, "December 11, 2018 landslide and 90-m icy tsunami in the Bureya water reservoir" in *Understanding and Reducing Landslide Disaster Risk: Volume 1 Sendai Landslide Partnerships and Kyoto Landslide Commitment*, K. Sassa, M. Mikoš, S. Sassa, P. T. Bobrowsky, K. Takara, K. Dang, Eds. (Springer, 2021), pp. 351–360.

ACKNOWLEDGMENTS

We are grateful to the boat captains and personnel who provided eyewitness reports of the tsunami. Any use of trade, firm, or product names is for descriptive purposes only and does not imply endorsement by the U.S. Government. We thank Sotiris Valkaniotis for valuable exchanges on photogrammetric processing, which helped us resolve processing blockages and improve our workflow. Peter Oswald and Julia Mickley of JOA Surveys are thanked for data access. **Funding:** Natural Sciences and Engineering Research Council 2020-04207 (D.H.S.); Alberta Innovates (D.H.S.); Canadian Space Agency (D.H.S.); U.S. Geological Survey Landslide Hazards Program (K.R.B., E.K.J., J.L., L.T.); NSF EAR-2314212 (M.B., G.H.R.); NSF CMMI-2603123 (P.L., B.H.); NERC Independent Research Fellowship (UKRI184, NE/B000184/1) (S.P.H.); U.S. Geological Survey G25AC00279-00 (E.K., M.W.); Eric and Wendy Schmidt AI in Science Postdoctoral Fellowship, a Schmidt Futures program (T.M.); Carlsberg Foundation CF24-2201 Reimagining Previously Glaciated Lands (K.S.). **Author contributions:** Note that after the lead author, author ordering is alphabetical. Conceptualization: D.H.S., M.B., M.G., P.L., G.H.R., K.S.; Data curation: D.H.S., K.R.B., M.B., A.F., S.P.H., E.K.J., P.L., J.L., T.M., M.V., M.E.W.; Formal analysis: D.H.S., K.R.B., M.B., J.C., G.E., A.F., S.P.H., B.H., E.K.J., E.K., P.L., J.L., T.M., G.H.R., K.S., L.T., M.V., M.E.W.; Investigation: D.H.S., K.R.B., M.B., J.C., G.E., A.F., M.G., S.P.H., B.H., E.K.J., E.K., P.L., J.L., T.M., G.H.R., K.S., L.T., M.V., M.E.W.; Methodology: J.C., S.P.H., E.K., P.L., T.M., M.V.; Projection administration: D.H.S.; Resources: D.H.S., A.F., P.L., J.L.; Software: K.R.B., M.B., A.F., P.L., T.M., G.H.R., M.V.; Validation: P.L., T.M.; Visualization: D.H.S., K.R.B., M.B., J.C., A.F., S.P.H., B.H., E.K.J., E.K., P.L., J.L., T.M., K.S., L.T., M.V.; Writing – original draft: D.H.S., K.R.B., M.B., J.C., A.F., M.G., S.P.H., E.K.J., E.K., P.L., J.L., T.M., G.H.R., K.S., L.T., M.V.; Writing – review and editing: D.H.S., K.R.B., M.B., J.C., G.E., A.F., M.G., S.P.H., B.H., E.K.J., E.K., P.L., J.L., T.M., G.H.R., K.S., L.T., M.V., M.E.W. **Competing interests:** Authors declare that they have no competing interests. **Data, code, and materials availability:** We used publicly available data sources whenever possible. Landsat data and historical air photos are available from (*73*), and Sentinel-2 data are available from (*74*). PlanetScope SuperDove satellite image data are available through Planet's Education and Research Program. Pre- and post-event very-high-resolution satellite images are available at a cost through Planet (Skysat) or Maxar/Vantor (Worldview, GeoEye). Imagery dates and details are provided in table S3. ArcticDEM data are available from (*35*). The DEM preparation workflow for SkySat imagery is available at (*75*), and the DEM alignment workflow is at (*76*). Ship traffic data are available upon request from Marine Exchange of Alaska (*28*). The SWOT high-rate pixel cloud data are available at (*63*). Tide gage data for the Juneau station (ID 9452210) are available at (*77*). Water level measurements in Endicott Arm from the Alaska Department of Natural Resources, NOAA grant number NA23NOS4690074, operated and maintained by JOA Surveys, are available from (*78*). The Berkeley Earth surface temperature data were obtained from (*79*). The merged TopoBathyDEM as well as field-surveyed runup elevations are available at (*78*). Seismic data from the following FDSN network codes were in this study: AK (*65*); CN (*66*); DK (*67*); G (*68*); GE (*69*); II (*70*); IU (*71*); US (*72*). Digitized trimline points from pre- and post-event satellite data are available as a shapefile at (*78*). Auxiliary files S1 to S7 are available at Zenodo (*78*). All other data needed to evaluate the conclusions in the paper are present in the paper or the supplementary materials. This study did not involve the sampling or generation of physical materials.

SUPPLEMENTARY MATERIALS

Submitted 22 September 2025; accepted 20 March 2026
Published online 6 May 2026
10.1126/science.aec3187

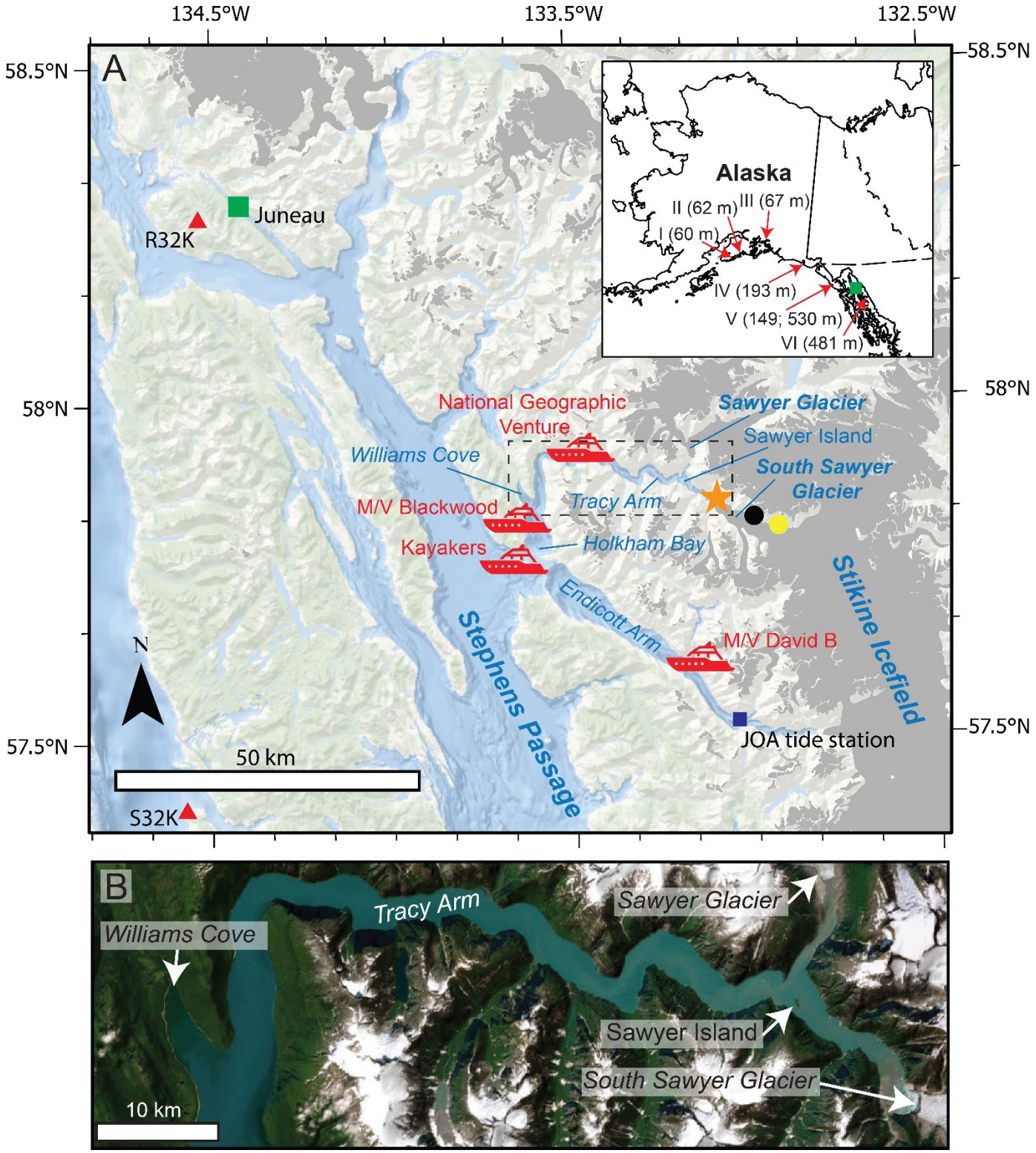

Fig. 1. Overview map of Tracy Arm and Endicott Arm in southeast Alaska. (**A**) Eyewitness locations shown with red ships, the nearest seismometers shown with red triangles, and city of Juneau, the only sizeable community in the map area, with green square (NOAA tide gage 9452210 is located here). Black and yellow circles indicate the seismic- and infrasound-derived landslide locations (respectively), and the orange star indicates the true location. Glaciers (gray) are from RGI-6.0 (*64*). Dashed black box shows extent of (B). Basemap is World Ocean Base from ArcGIS Pro (Sources: Esri, TomTom, Garmin, GEBCO, National Geographic, NOAA, and the GIS User Community, CHS, Esri, GEBCO, Garmin, NaturalVue). Inset map points to Juneau (green square) and locations of landslide-tsunamis in the past century with over 50 m runup (refer to table S1) as follows: Grewingk Lake, 1960 (I); Pedersen Lagoon, 2024 (II); Cliff Mine, 1964 (III); Taan Fiord, 2015 (IV); Lituya Bay, 1936, 1958 (V); and Tracy Arm, 2025 (VI). (**B**) Satellite basemap image of Tracy Arm showing locations of Sawyer and South Sawyer glaciers, Sawyer Island, and Williams Cove. Orange star indicates location of the landslide. Basemap is World Imagery in ArcGIS Pro (Sources: Earthstar Geographics).

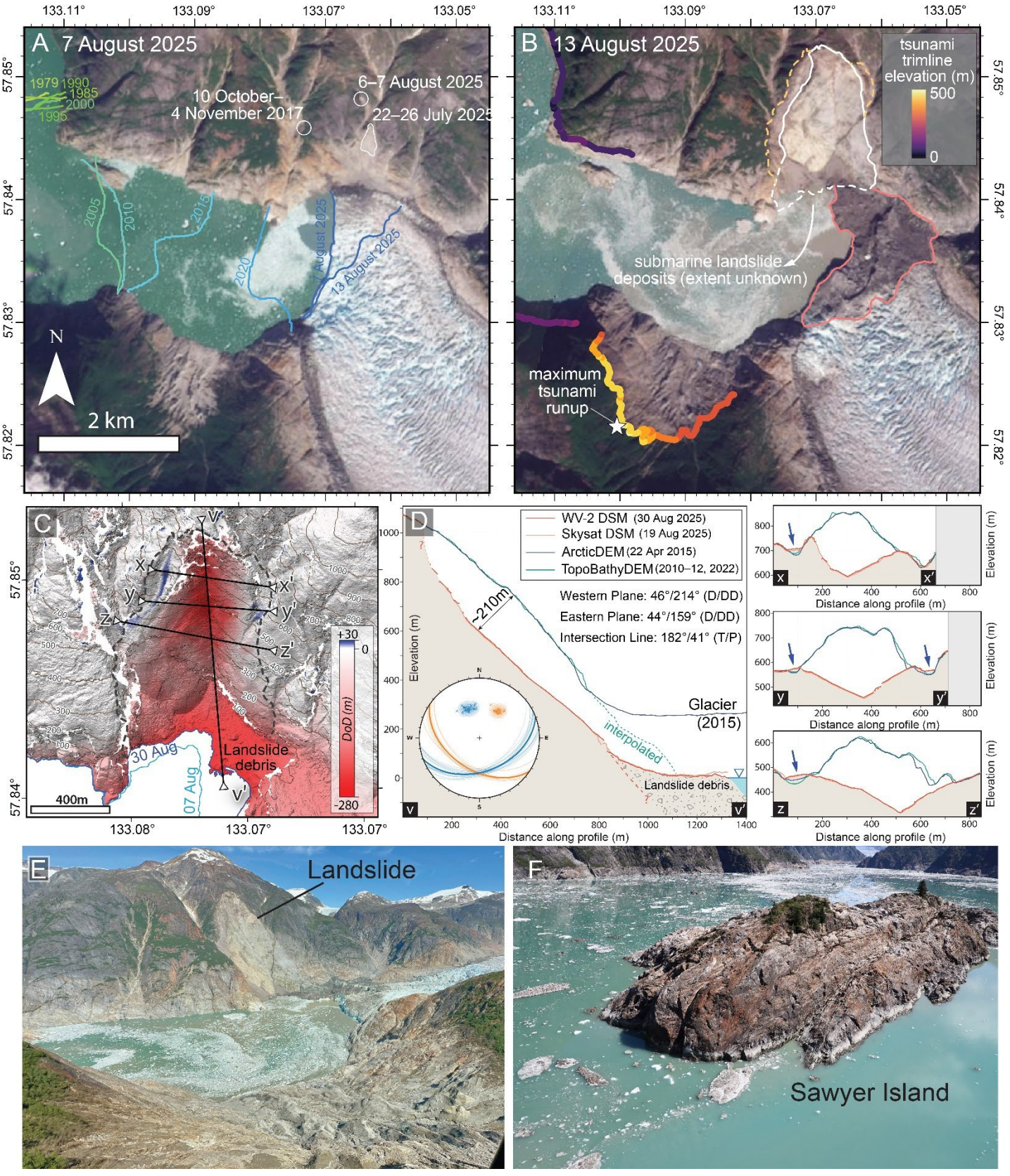

Fig. 2. Overview of the Tracy Arm landslide and tsunami. (**A**) Pre- and (**B**) post-event satellite images (© 2025 Planet Labs PBC) showing the location and extent of the Tracy Arm landslide. South Sawyer Glacier terminus positions since 1979 (green to blue lines) and the locations of three precursor slope failures (white outlines) since 2017 are shown in (A). (B) shows the landslide source (white line) and deposit areas (pink line) and mapped tsunami runup elevations (colored dots), including the location of maximum tsunami runup on the opposite side of the fiord (white star). The mapped trimline is a minimum estimate of the maximum wave runup because higher water may have been non-destructive. The dashed white line indicates the visible distal extent of the landslide because the source area likely extended below sea level and the dashed orange line indicates the landslide affected area, including secondary failures. (**C**) Elevation change (m) from the digital elevation model (DEM)-of-Difference (DoD) overlain on the post-landslide 2-m WorldView-2 DEM (table S3), highlighting the landslide scar and the onshore debris whose subaqueous extent is unknown. Pre- and post-event coastlines are outlined in light- and dark-blue lines, respectively. Dashed black line indicates the union of the white and orange dashed lines in (B). (**D**) Along- and cross-wedge profiles of the pre- and post-event DEMs and digital surface models (DSM), respectively [locations in (C); elevation is m above sea level]. The axial profile v–v′ captures the maximum normal thickness of the 10 August 2025 landslide source, in terms of elevation change (m) with respect to 2015 and 2025 DEMs. Blue arrows in the right-most profiles indicate peripheral deposition. The inset lower-hemispheric stereonet summarizes the orientations of the western (blue) and eastern (orange) planes. Dashed red line indicates a plausible but unknown bedrock elevation. D/DD is dip angle and dip direction, whereas T/P refers to trend and plunge. (**E**) Oblique aerial photo from above the highest runup point looking north toward the landslide, with South Sawyer Glacier on the right side. (Photo credit: John Lyons, U.S. Geological Survey). (**F**) Oblique aerial photo of Sawyer Island looking toward the east, showing the surviving patch of vegetation on the island's high point (Photo credit: John Lyons, U.S. Geological Survey).

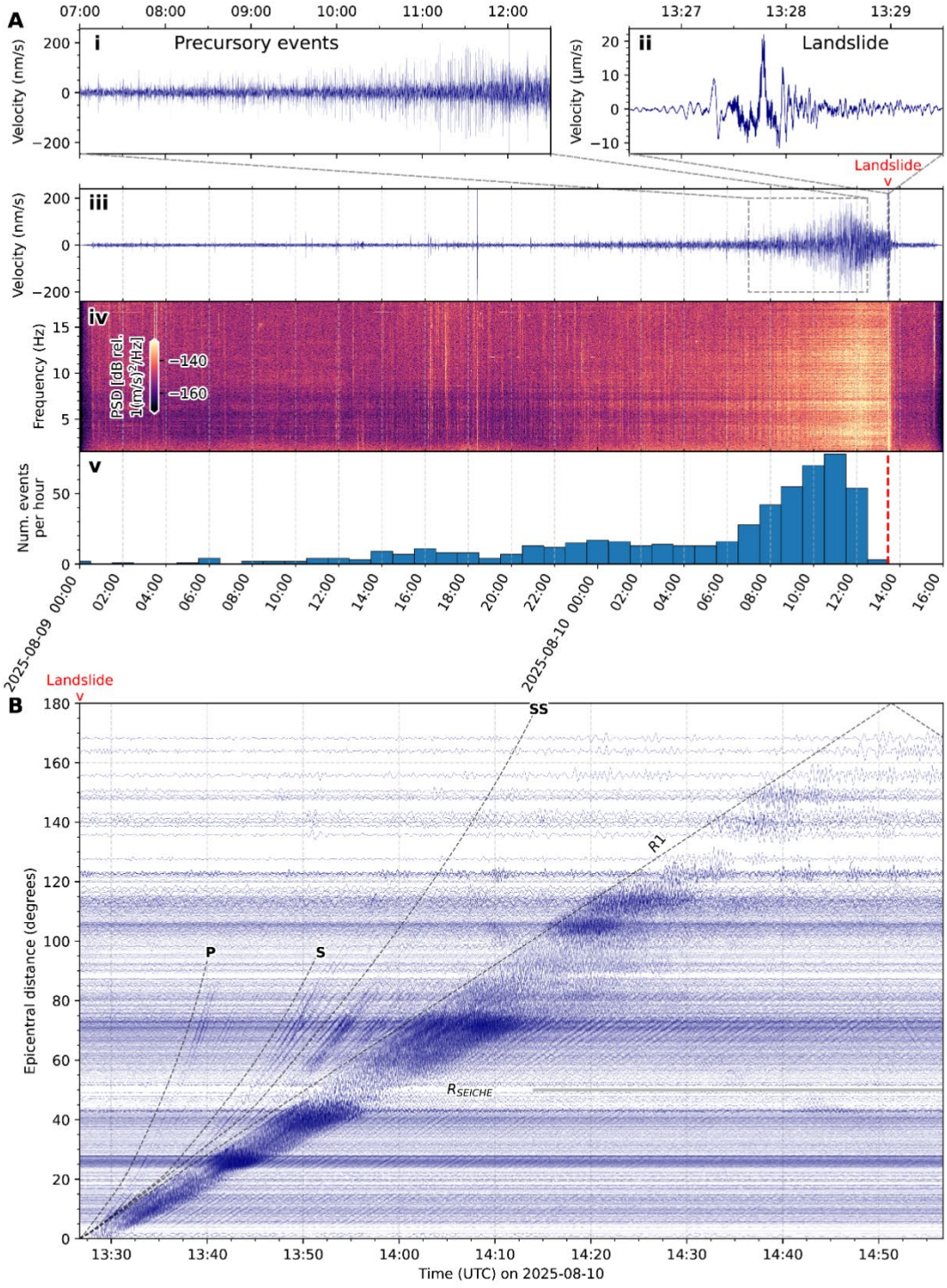

Fig. 3. Pre- and co-landslide seismic signals. (**A**) Waveform and spectrogram from station AK.S32K (location shown in Fig. 1) showing precursory seismicity. (i) Time series of rapidly occurring precursory earthquakes recorded over ~6 hours prior to the landslide (waveform bandpass filtered 2.5–8 Hz). (ii) The seismic signal of the landslide; note the difference in vertical scale relative to the precursors (unfiltered waveform). (iii) Waveform for the ~36 hours prior to the landslide (bandpass filtered 2.5–8 Hz). (iv) Spectrogram for the same window of seismic data; precursory events are visible as narrow, high-frequency (2 –20 Hz) pulses, which become more tremor-like in the hour before failure. (v) Hourly number of precursory earthquakes, which rapidly increases in the hours prior to the landslide at 13:26 UTC (dashed line). (**B**) Vertical-component seismic record section from broadband stations around the world [AK (*65*); CN (*66*); DK (*67*); G (*68*); GE (*69*); II (*70*); IU (*71*); US (*72*)], showing body (P, S, SS) and surface Rayleigh waves (R1, R2) from the landslide, out of which long-period (~66 s) lower amplitude waves emerge (R_{SEICHE}). Waveforms are bandpass filtered between 15 and 70 s.

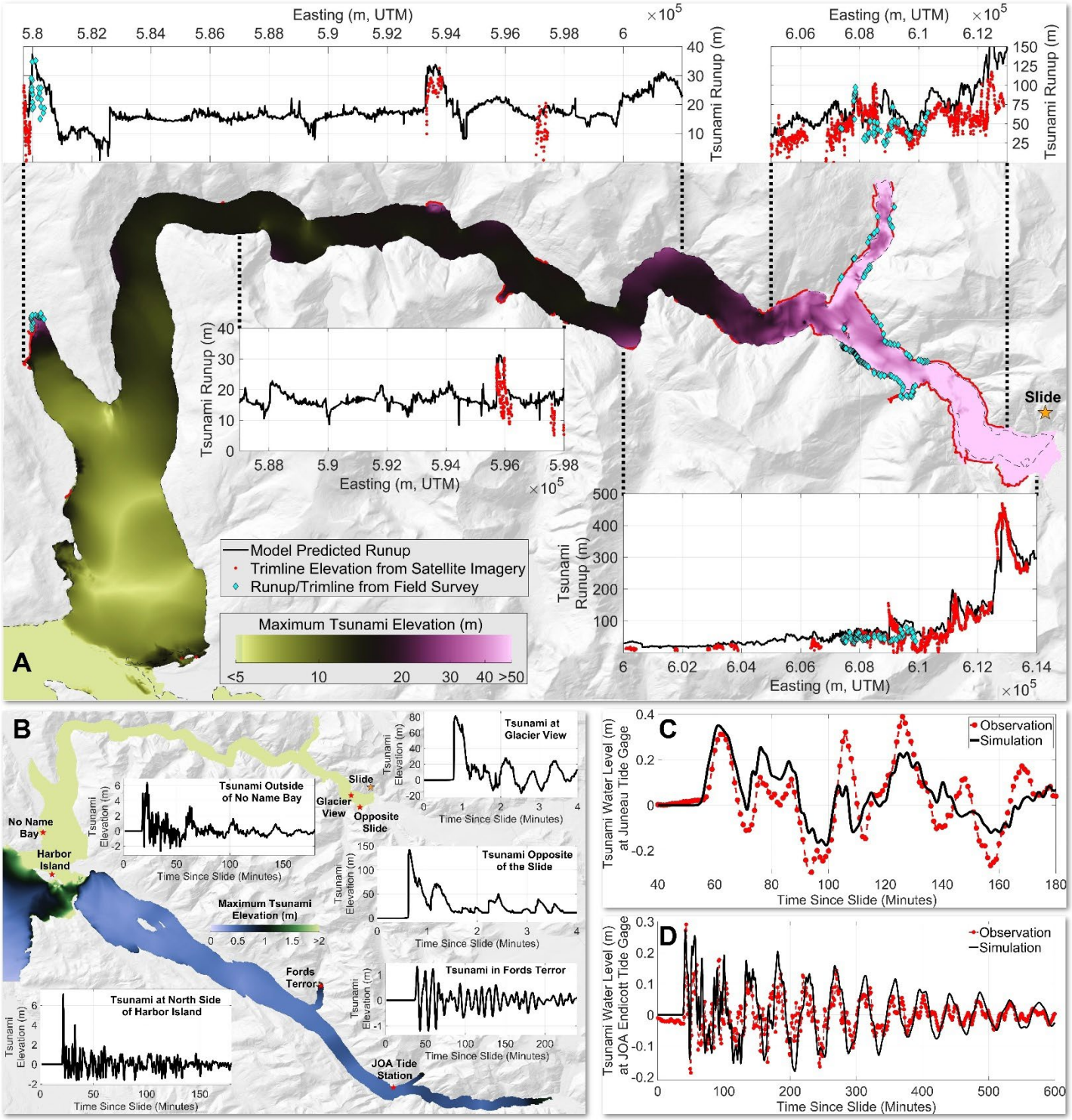

Fig. 4. Summary of the tsunami simulation - observation comparisons. (A) Tsunami elevations and runup in Tracy Arm. The maximum tsunami elevation from the numerical model is shown in the map view, with red lines indicating the locations of tsunami trimlines from satellite imagery and the light blue diamonds indicating the runup measured during the field survey. The inset panels above and below provide comparisons between the model-predicted runup (black lines) and the satellite-inferred trimline/runup (red dots/blue diamonds) along the northern and southern shorelines of Tracy Arm, respectively. (B) Tsunami simulation results in Tracy Arm and Endicott Arm. Time series of the tsunami elevation are shown from various locations indicated by the red stars. (C) Model (black line) comparison with the tide gage data (red dots) from the NOAA Juneau tide gage, which records a water level observation every 1 min. (D) Model (black line) comparison with the JOA tide gage data (red dots) from Endicott Arm, sampled every 1 min. Refer to Data, code, and materials availability for tide gage information. Basemaps are hillshades from the TopoBathyDEM (refer to Data, code, and materials availability).

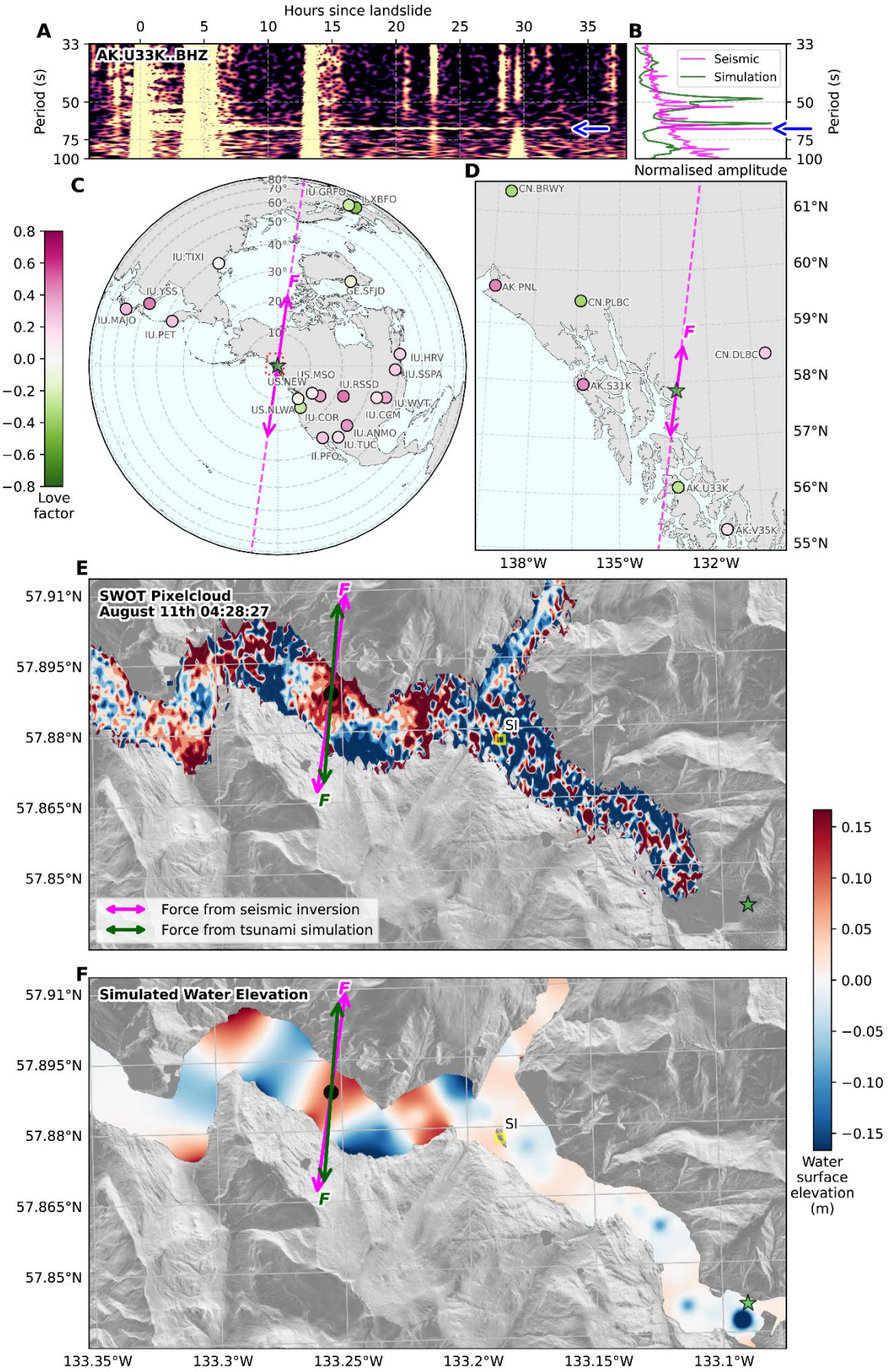

Fig. 5. Observations and modeling of a 66-s period landslide-induced seiche in Tracy Arm. (**A**) Spectrogram of long-period vertical component seismic data from AK.U33K [location in (D)] showing a 66 s period signal (highlighted by blue arrow) persisting for >30 hours post-landslide. (**B**) Averaged three-component seismic amplitude spectrum from all stations shown in (C) and (D) for a 2 hours window beginning 1 hour after the landslide (pink line), compared with a spectral average of virtual tide gage time series from the tsunami simulation (green line). Both spectra are self-normalized. (**C**) and (**D**) show surface wave radiation patterns of the 66 s period signal observed by seismic stations at regional and teleseismic distances, respectively, as quantified by Love Factor values (*60*). (**E**) Surface Water Ocean Topography (SWOT) Pixel cloud observations of sea-surface height approximately 20 hours after the landslide occurred (11 August, 04:28:27 UTC). (**F**) Simulated sea-surface height from tsunami model 8 hours after landslide occurrence. The pink arrow in (C) to (F) indicates the oscillating single-force azimuth from inversion of regional 66 s period seismic waveforms; the green arrow in (E) and (F) is the maximum horizontal pressure of the 66 s seiche from the tsunami model. Basemaps for (E) and (F) are hillshades from ArcticDEM (*35*).

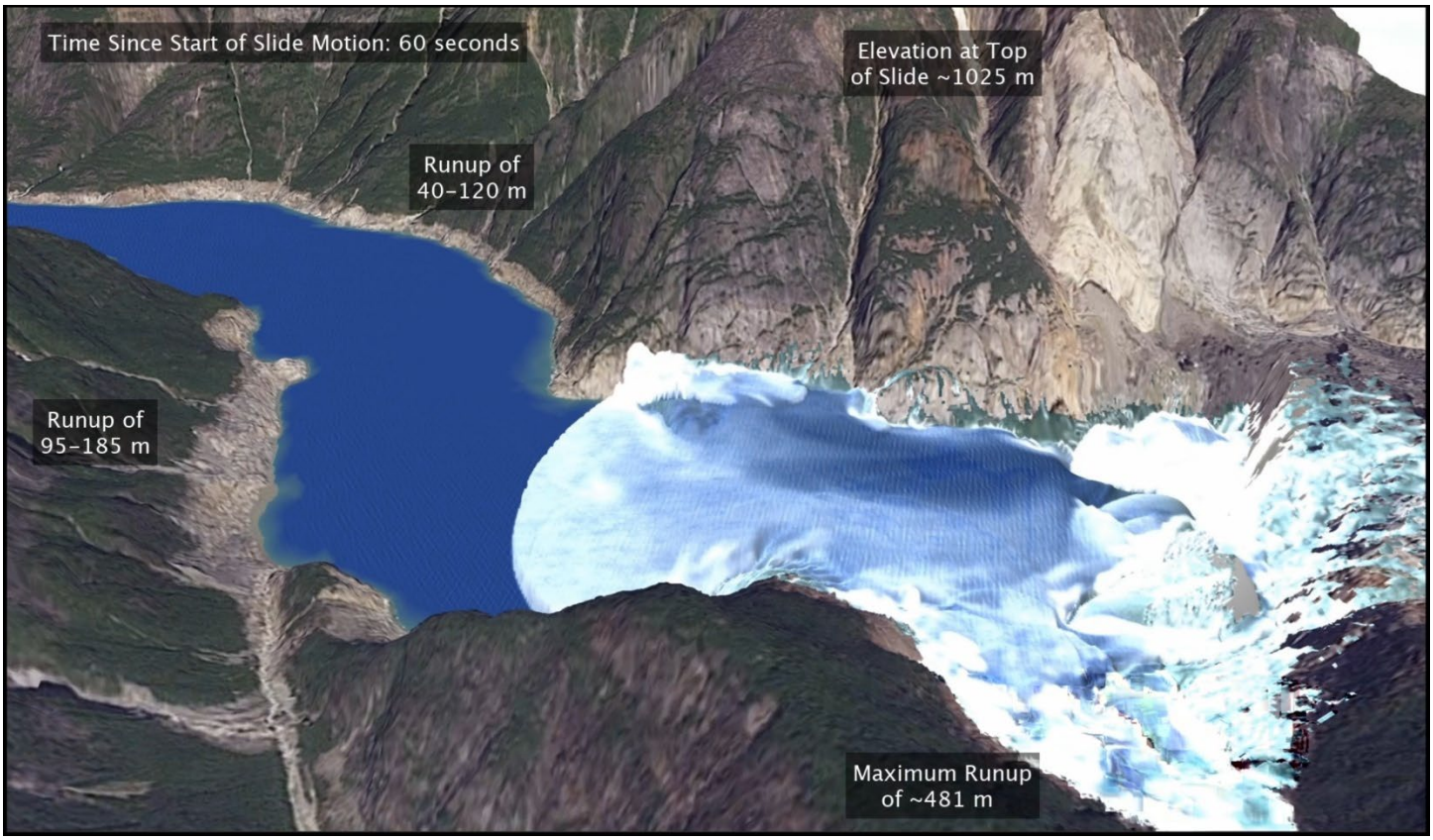

Movie 1. A near-source animation of the tsunami generated by the Tracy Arm landslide. The tsunami is shown with a photorealistic render and the post-event Planet SuperDove satellite imagery (table S3) draped over topography. Annotations of runup provide satellite-derived trimline elevations. Animation begins with a perspective view of the landslide- and tsunami-impacted areas, shown at a time before the landslide has started to move; at ~30 s after the start of landslide motion, when roughly ¾ of the landslide volume is in the water and a large breaking tsunami with crest elevation of 125 m has been generated; at 1 min, when the tsunami nears maximum runup on the opposite slope and a large breaking bore is headed down Tracy Arm; and the return flow from the maximum runup location sloshes back toward the source area, likely reworking the slide deposits in the area. At 90 s, the tsunami runs ≥150 m up a slope 3 km from the landslide. The tsunami continues down Tracy Arm, with strong amplification along a southern shoreline river mouth with maximum runup near 150 m, before reaching Sawyer Island 3.5 min after the start of landslide motion. Here the tsunami energy splits, with energy continuing to the west in the main Tracy Arm channel and energy traveling northward toward Sawyer Glacier, where runup elevations again exceed 100 m.

A 481-meter-high landslide-tsunami in a cruise ship–frequented Alaska fjord

Dan H. Shugar, Katherine R. Barnhart, Mira Berdahl, Jacqueline Caplan-Auerbach, Göran Ekström, Aram Fathian, Marten Geertsema, Stephen P. Hicks, Bretwood Higman, Erin K. Jensen, Ezgi Karasözen, Patrick Lynett, John Lyons, Thomas Monahan, Gerard Roe, Kristian Svennevig, Liam Toney, Maximillian Van Wyk de Vries, and Michael E. West

*Science***Ahead of Print** DOI: 10.1126/science.aec3187